











**Two types of colossal magnetoresistance with distinct mechanisms in  $\text{Eu}_5\text{In}_2\text{As}_6$** 

Sudhaman Balguri <sup>1,\*</sup>, Mira B. Mahendru <sup>1,\*</sup>, Enrique O. González Delgado <sup>1</sup>, Kyle Fruhling <sup>1</sup>, Xiaohan Yao <sup>1</sup>,  
David E. Graf,<sup>2</sup> Jose A. Rodríguez-Rivera <sup>3,4</sup>, Adam A. Aczel <sup>5</sup>, Thomas J. Hicken,<sup>6</sup> Hubertus Luetkens,<sup>6</sup>  
Michael J. Graf,<sup>1</sup> Andreas Rydh <sup>7</sup>, Jonathan Gaudet <sup>3,4</sup> and Fazel Tafti <sup>1,†</sup>

<sup>1</sup>*Department of Physics, Boston College, Chestnut Hill, Massachusetts 02467, USA*

<sup>2</sup>*National High Magnetic Field Laboratory, Tallahassee, Florida 32310, USA*

<sup>3</sup>*NIST Center for Neutron Research, National Institute of Standards and Technology, Gaithersburg, Maryland 20899, USA*

<sup>4</sup>*Department of Materials Science and Engineering, University of Maryland, College Park, Maryland 20742-2115, USA*

<sup>5</sup>*Neutron Scattering Division, Oak Ridge National Laboratory, Oak Ridge, Tennessee 37831, USA*

<sup>6</sup>*Laboratory for Muon Spin Spectroscopy (LMU), Paul Scherrer Institute (PSI), CH-5232 Villigen, Switzerland*

<sup>7</sup>*Department of Physics, Stockholm University, 106 91 Stockholm, Sweden*



(Received 12 December 2024; accepted 14 February 2025; published 5 March 2025)

Recent reports of colossal negative magnetoresistance (CMR) in a few magnetic semimetals and semiconductors have attracted attention because these materials are devoid of the conventional mechanisms of CMR such as mixed valence, double-exchange interaction, and Jahn-Teller distortion. New mechanisms have thus been proposed, including topological band structure, ferromagnetic clusters, orbital currents, and charge ordering. The CMR in these compounds has been reported in two forms: either a resistivity peak or a resistivity upturn suppressed by a magnetic field. Here we reveal both types of CMR in a single antiferromagnetic semiconductor  $\text{Eu}_5\text{In}_2\text{As}_6$ . Using the transport and thermodynamic measurements, we demonstrate that the peak-type CMR is likely due to the percolation of magnetic polarons with increasing magnetic field, while the upturn-type CMR is proposed to result from the melting of a charge order under the magnetic field. We argue that similar mechanisms operate in other compounds, offering a unifying framework to understand CMR in seemingly different materials.

DOI: [10.1103/PhysRevB.111.115114](https://doi.org/10.1103/PhysRevB.111.115114)

**I. INTRODUCTION**

Antiferromagnetic (AFM) materials with coupled charge, spin, and lattice degrees of freedom are coming to the forefront of electronic, spintronic, and caloritronic applications [1–3]. The Eu-based Zintl compounds are emerging as a fascinating family of functional AFM semiconductors with intertwined degrees of freedom. They exhibit exotic properties such as fluctuating Weyl nodes in  $\text{EuCd}_2\text{As}_2$  [4,5], axion insulator phase in  $\text{EuIn}_2\text{As}_2$  [6,7], and colossal magnetoresistance (CMR) in  $\text{EuCd}_2\text{P}_2$  [8–10] and  $\text{Eu}_5\text{In}_2\text{Sb}_6$  [11–15]. Since CMR is particularly applicable in sensing and logic devices, it has been sought in a variety of materials including the chalcogenide Zintl phase  $\text{Mn}_3\text{Si}_2\text{Te}_6$  [16] and Dirac semimetals such as  $\text{CeSbTe}$  and  $\text{EuAuSb}$  [17,18]. The general features of CMR in these materials are similar; they all exhibit a peak in their zero-field resistivity curves  $\rho(T)$  which is suppressed by an external magnetic field. In some cases, such as  $\text{Eu}_5\text{In}_2\text{Sb}_6$  and  $\text{Mn}_3\text{Si}_2\text{Te}_6$ , a sharp upturn is observed in  $\rho(T)$  at low temperatures which is also suppressed by the magnetic field. Different mechanisms have been proposed for either type of CMR (peak or upturn), including ferromagnetic (FM) clusters [9], band structure reconstruction [19], chiral orbital currents [16], and interplay between Dirac fermions and charge ordering [17].

Here, we reveal both types of CMR in a single AFM semiconductor  $\text{Eu}_5\text{In}_2\text{As}_6$  and discuss the underlying mechanism for each type. A few properties of the title compound make it ideal for understanding CMR in the context of other related materials mentioned above. First,  $\text{Eu}_5\text{In}_2\text{As}_6$  is topologically trivial as shown by recent first-principles calculations [20], so Dirac fermions are irrelevant to its CMR, unlike the proposals for  $\text{CeSbTe}$  and  $\text{EuAuSb}$  [17,18]. Second,  $\text{Eu}_5\text{In}_2\text{As}_6$  is a semiconductor with a band gap of 35 meV corresponding to temperature and field scales of about 400 K and 300 T. Thus, its sharp resistivity upturn at 15.5 K which is completely suppressed by 9 T, as shown here, cannot be due to a field- or temperature-induced transition from an insulator to a metal. Third,  $\text{Eu}^{2+}$  ions in  $\text{Eu}_5\text{In}_2\text{As}_6$  are not at the center of high-symmetry anionic polyhedra, so they are not subjected to orbital currents as proposed for  $\text{Mn}_3\text{Si}_2\text{Te}_6$  [16].

In this work, we argue that the peaklike CMR in  $\text{Eu}_5\text{In}_2\text{As}_6$  at high temperatures is related to polaron physics while the upturnlike CMR at low temperatures is potentially related to charge segregation or charge ordering. The extremely large magnitudes of both effects indicate a strong coupling among charge, spin, and lattice degrees of freedom, a property that could be common among the Zintl compounds mentioned above.

**II. METHODS**

Polycrystalline samples of  $\text{Eu}_5\text{In}_2\text{As}_6$  have been previously synthesized [21,22] but single crystals were not

\*These authors contributed equally to this work.

†Contact author: fazel.tafti@bc.edu

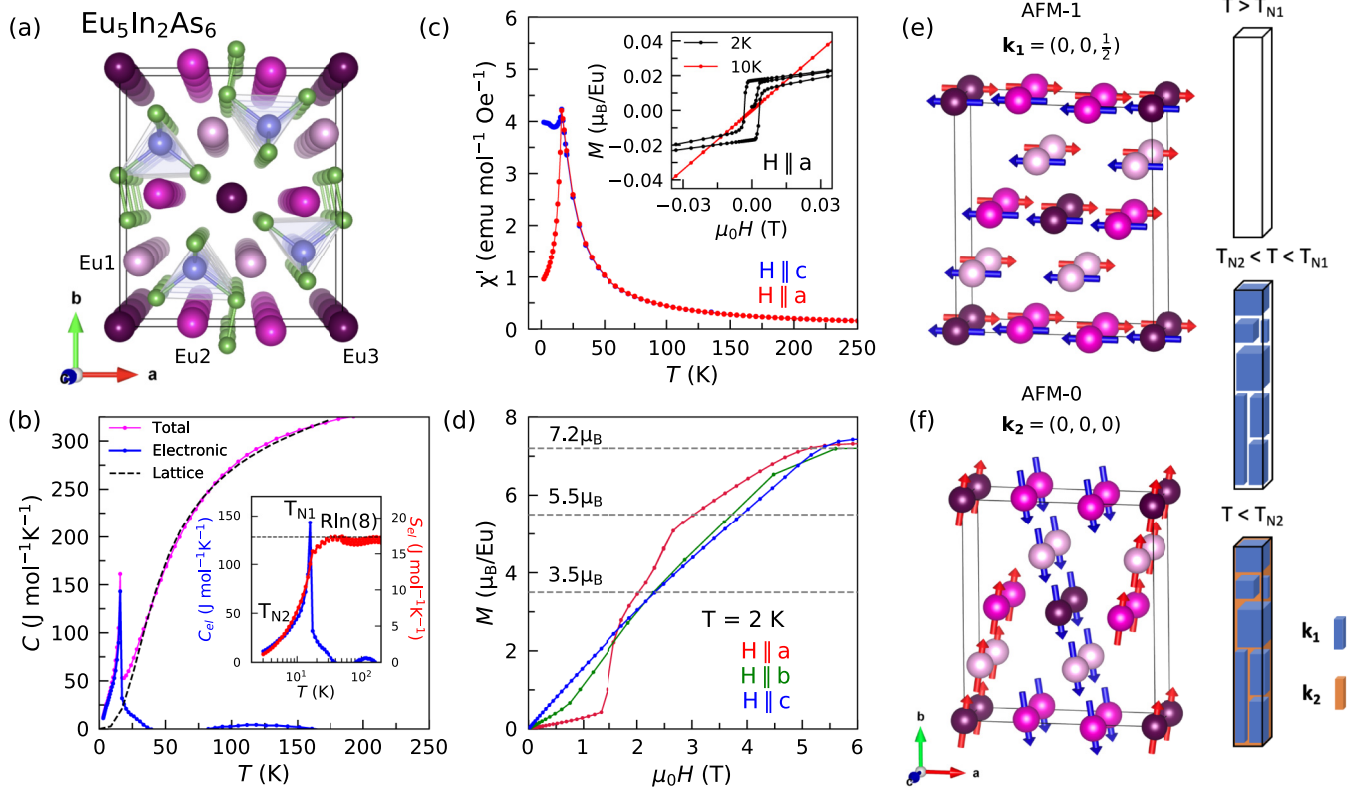


FIG. 1. (a) Orthorhombic unit cell of  $\text{Eu}_5\text{In}_2\text{As}_6$  in the space group  $Pbam$ . (b) Total, electronic, and lattice heat capacity shown in magenta, blue, and black colors. The lattice background is modeled assuming anharmonic Debye model [23,24] with  $\Theta_D = 196$  K. Inset shows the electronic heat capacity (blue) and entropy (red). (c) AC magnetic susceptibility curves suggest AFM ordering with in-plane moments and alternating direction along the  $c$  axis. The hysteresis loop at  $T < T_{N2}$  in the inset suggests FM ordering along the  $a$  axis. (d) Three steps in the  $M(H)$  curve when  $H \parallel a$  suggest spin flops on different Eu sites. (e) The AFM spin structure determined by neutron diffraction in Sec. III E at  $T < T_{N1}$ . The ordered moments are FM aligned along the  $a$  axis and AFM aligned along the  $c$  axis. The AFM-1 structure persists to zero temperature. (f) At  $T < T_{N2}$ , new magnetic domains with  $\mathbf{k}_2 = (0, 0, 0)$  emerge in separate regions of the sample. According to the analysis of (b), these domains (AFM-0) constitute less than 20% of the sample volume. The diagram on the right shows the phase separation scenario where the  $\mathbf{k}_2$  domains nucleate from the domain walls of the  $\mathbf{k}_1$  order.

available until now. We report the first crystal growth of this compound here (see Supplemental Material [24]). Powder x-ray diffraction was performed using a Bruker D8 ECO instrument. The FULLPROF suite [25] and VESTA software [26] were used for the Rietveld refinement and crystal visualization. Physical properties were measured using Quantum Design Dynacool-PPMS and MPMS-3.

Neutron diffraction data were collected using the thermal neutron triple-axis spectrometer VERITAS at the High Flux Isotope Reactor (HFIR) in Oak Ridge National Laboratory. A few crystals were mounted on an Al plate with either the  $c$  axis or  $b$  axis perpendicular to the scattering plane to probe the  $(H, K, 0)$  or  $(H, 0, L)$  Bragg peaks, respectively. Representation analysis was performed using SARAH [27]. The Cooper-Nathans formalism was used to calculate the resolution function of VERITAS [28], and the Wuesch-Prewitt algorithm [29] was used to calculate the angle-dependent neutron transmission of the sample. The statistical error for each intensity point corresponds to 1 standard deviation.

The  $\mu\text{SR}$  data were taken on the general purpose surface-muon spectrometer at the  $\pi\text{M3}$  beam line of the Swiss Muon Source at the Paul Scherrer Institute [30].

### III. RESULTS AND DISCUSSION

#### A. Structural analysis

From a chemical standpoint,  $\text{Eu}_5\text{In}_2\text{As}_6$  is considered a Zintl compound, i.e., it is an intermetallic material that exhibits semiconducting behavior due to the charge balance between large cationic and anionic complexes that make up its lattice structure [31]. In this compound, the positive charge of  $[\text{Eu}_5]^{10+}$  is balanced by the negative charges of  $[\text{In}_2\text{As}_4]^{6-}$  and  $[\text{As}_2]^{4-}$  complexes [32].

$\text{Eu}_5\text{In}_2\text{As}_6$  has an orthorhombic unit cell with three inequivalent Eu sites and a characteristic chain stacking of atoms as shown in Fig. 1(a). Details of the x-ray refinement are presented in the Supplemental Material Fig. S1 and Tables S1 and S2 [24]. The crystal structure of  $\text{Eu}_5\text{In}_2\text{As}_6$  belongs to the same nonsymmorphic space group  $Pbam$  (No. 55) as its sister compounds  $\text{Ba}_5\text{In}_2\text{Sb}_6$  and  $\text{Eu}_5\text{In}_2\text{Sb}_6$ , which are predicted to be topological hourglass and axion insulators, respectively [11,33].

A recent density functional theory (DFT) calculation shows that while  $\text{Eu}_5\text{In}_2\text{Sb}_6$  and  $\text{Eu}_5\text{In}_2\text{Bi}_6$  could be topological,  $\text{Eu}_5\text{In}_2\text{As}_6$  is a trivial semiconductor [20]. We specifically

chose this compound to demonstrate that a large CMR does not rely on topological aspects of the band structure. This is important because the salient features of CMR in the trivial semiconductor  $\text{Eu}_5\text{In}_2\text{As}_6$  are similar to those in topological systems such as the Dirac semimetals  $\text{CeSbTe}$  and  $\text{EuAuSb}$  [17,18], Weyl semimetal  $\text{EuCd}_2\text{As}_2$  [4], and axion insulator  $\text{Eu}_5\text{In}_2\text{Sb}_6$  [15].

Another exotic mechanism proposed for CMR is the modification of chiral orbital currents (COC) in  $\text{Mn}_3\text{Si}_2\text{Te}_6$  with applied field [16]. Central to this mechanism is the octahedral coordination of six Te atoms around each  $\text{Mn}^{2+}$  ion, enabling the interaction between the COC and  $\text{Mn}^{2+}$  spin. As seen in Fig. 1(a), the  $\text{Eu}^{2+}$  ions in  $\text{Eu}_5\text{In}_2\text{As}_6$  are not directly surrounded by a high-symmetry polyhedron of In and As. Therefore, COC is not a viable mechanism for the CMR in  $\text{Eu}_5\text{In}_2\text{As}_6$ .

The above structural analysis dismisses topology and COC as the source of CMR in  $\text{Eu}_5\text{In}_2\text{As}_6$ . Next, we will discuss its magnetic structure and phase diagram, before a detailed analysis of CMR.

### B. Magnetic transitions

The heat-capacity data in Fig. 1(b) reveal two AFM transitions in zero field at  $T_{N1} = 16.0(2)$  K and  $T_{N2} = 5.4(3)$  K. Magnetism is driven by  $\text{Eu}^{2+}$  ions in the half-filled  $4f^7$  configuration ( $^8S_{7/2}$ ) with  $L = 0$  and  $S = \frac{7}{2}$ , consistent with the saturated entropy  $R \ln(8) \text{ Jmol}^{-1} \text{ K}^{-1}$  in the inset of Fig. 1(b), saturated magnetization  $7.2\mu_B$  in Fig. 1(d), and effective moment  $\mu_{\text{eff}} = 7.8(6)\mu_B$  from a Curie-Weiss analysis in Fig. S2 [24].

The inset of Fig. 1(b) shows that approximately 10% of the full entropy is released by  $T_{N2}$ , 70% is released between  $T_{N2}$  and  $T_{N1}$ , and 20% is released above  $T_{N1}$ . For comparison,  $\text{Eu}_5\text{In}_2\text{Sb}_6$  also exhibits two transitions at  $T_{N1} = 14$  K and  $T_{N2} = 7$  K but it releases about 40% of entropy at each transition and 20% above  $T_{N1}$  [13]. In both materials, 20% of total entropy is released above  $T_{N1}$ , suggesting short-range magnetic correlations (polarons) that survive up to  $3T_{N1}$  [34,35].

Temperature dependence of the in-plane and out-of-plane magnetic susceptibility in Fig. 1(c) suggests an AFM order with the moments in the  $ab$  plane but alternating along the  $c$  axis. The inset of Fig. 1(c) shows the absence of a hysteresis loop at  $T_{N2} < T < T_{N1}$ , so the order is purely AFM in this temperature range. However, a small hysteresis loop opens below  $T_{N2}$  when  $H \parallel a$ , suggesting a finite in-plane FM component when  $T < T_{N2}$ .

The behavior of  $M(H)$  curves along three different crystallographic directions is shown in Fig. 1(d). When  $H \parallel c$ , the  $M(H)$  curve is strictly linear, indicating a continuous rotation of spins from  $ab$  plane toward  $c$  axis with increasing field. In contrast, the  $M(H)$  curve exhibits three steps when  $H \parallel a$ , indicating consecutive spin flops on different Eu sites within the  $ab$  planes. The steps are less apparent when  $H \parallel b$ , suggesting that the  $a$  axis is the easy axis. A positive Curie-Weiss temperature ( $\Theta_{\text{CW}} = +15$  K) in Fig. S2 [24] indicates FM correlations despite an AFM order, consistent with FM correlations within the  $ab$  planes in spite of AFM ordering along the  $c$  axis.

The spin structure at zero field is discussed in Sec. III E. While we cannot rule out the possibility that both magnetic ordering at  $T_{N1}$  and  $T_{N2}$  form within the same magnetic domain, we suggest an alternative scenario where spatially separated magnetic domains form below each transition temperature. In this scenario, an AFM-1 spin structure [Fig. 1(e)] appears below  $T_{N1}$  and occupies the entire sample volume according to our Supplemental Material  $\mu\text{SR}$  data (Fig. S6 [24]). The AFM-1 spin structure is obtained from neutron diffraction analysis explained in Sec. III E. It has FM spins within the  $ab$  planes with an easy  $a$  axis and alternating spin direction between adjacent planes along the  $c$  axis. This structure is consistent with the  $\chi(T)$  and  $M(H)$  curves shown in Figs. 1(c) and 1(d). Then, at  $T < T_{N2}$ , a different ordered structure [AFM-0 in Fig. 1(f)] appears in less than 20% of the sample volume, consistent with our entropy analysis in the inset of Fig. 1(b). Most likely, AFM-0 nucleates from the domain walls of AFM-1. This spin structure has an FM component along the  $a$  axis, which explains the hysteresis observed in the inset of Fig. 1(c) at 2 K. Ferromagnetism along the  $a$  axis was also observed in the sister compound  $\text{Eu}_5\text{In}_2\text{Sb}_6$ , but is only stabilized for  $T_{N2} < T < T_{N1}$  [11,13,15].

### C. Phase diagrams

We used detailed measurements of the AC susceptibility and nanocalorimetry to map the temperature-field phase diagram of  $\text{Eu}_5\text{In}_2\text{As}_6$ . Figure 2(a) shows three characteristic fields ( $H_1$ ,  $H_2$ , and  $H_3$ ) in the AC susceptibility data at  $T = 2$  K. They coincide with the three steps in the  $M(H \parallel a)$  curve in Fig. 1(d). With increasing temperature, these characteristic fields become smaller and merge as shown in the phase diagram of Fig. 2(c). The triangular data points that define the outer boundary of the  $H \parallel a$  phase diagram indicate the field dependence of  $T_{N1}$  in the heat-capacity data [Fig. 2(b)]. The  $T_{N2}$  phase boundary is determined via a low-temperature nanocalorimetry technique [36] shown in Fig. S3 (see also the Supplemental Material tunnel diode oscillation data in Figs. S4 and S5 [24]). The striped region on the phase diagrams of Fig. 2(c) indicates the phase separation between AFM-0 and AFM-1 spin structures in different regions of the sample with AFM-1 being the majority domain.

The phase diagram of Fig. 2(c) shows that the AFM-1 phase transitions into AFM-2 and AFM-3 with increasing field when  $H \parallel a$ . Given that  $\text{Eu}_5\text{In}_2\text{As}_6$  has three Eu sites in the unit cell [Fig. 1(a)], and considering the three metamagnetic steps in the  $M(H)$  curve when  $H \parallel a$  [Fig. 1(d)], we conclude that the AFM-2 and AFM-3 phases correspond to consecutive spin flips on the Eu1 and Eu2 sites, respectively. This is schematically presented in Fig. S5. Since the spins are oriented along the  $\pm a$  axis in the AFM-1 phase [Fig. 1(e)], an applied field along the  $c$  axis will continuously rotate them out of the  $ab$  plane without spin flips. This explains the linear  $M(H)$  behavior when  $H \parallel c$  in Fig. 1(d) and the absence of AFM-2 and AFM-3 phases in the phase diagram of Fig. 2(f) with  $H \parallel c$ .

The AC susceptibility and heat-capacity data for  $H \parallel c$  in Figs. 2(d) and 2(e) are used to map the phase diagram

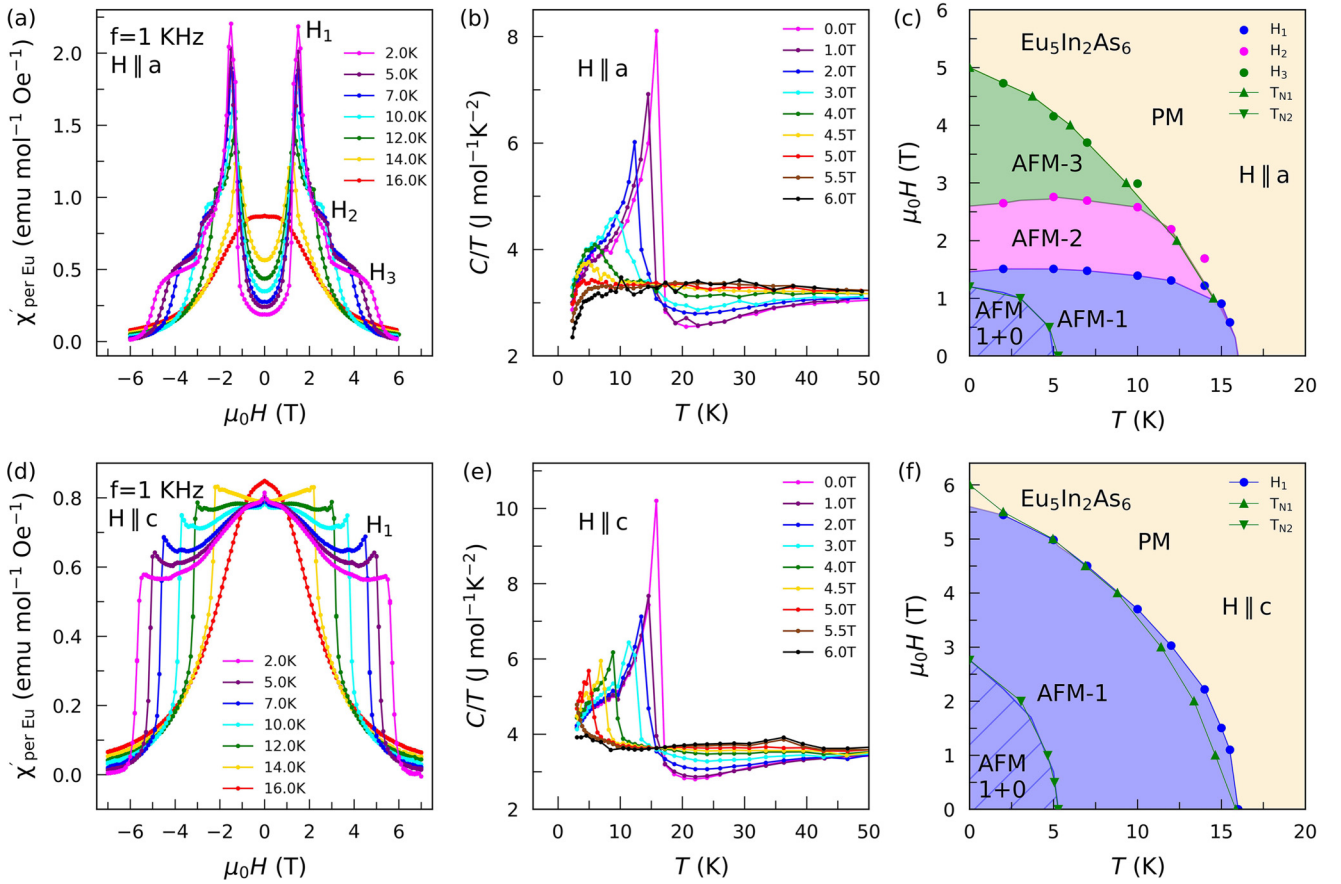


FIG. 2. (a) Field dependence of the real part of the AC susceptibility  $\chi'(H)$  at several temperatures. The  $H_1$ ,  $H_2$ , and  $H_3$  features imply spin-flop transitions. They correspond to the three steps in DC magnetization in the red curve on Fig. 1(d). (b) Temperature dependence of the heat capacity at several magnetic fields. The sharp peak marks  $T_{N1}$ . (c) The magnetic phase diagram when  $H \parallel a$ . The area marked by striped lines indicates the coexistence of AFM-0 and AFM-1 domains [Figs. 1(e) and 1(f)] in separate regions of the sample. (d)–(f) Similar data and phase diagram to (a)–(c) when  $H \parallel c$ .

with out-of-plane field in Fig. 2(f). Supplemental Material nanocalorimetry data in Fig. S3 are used to define the  $T_{N2}$  boundary when  $H \parallel c$ . The rich phase diagrams of Figs. 2(c) and 2(f) suggest that  $\text{Eu}_5\text{In}_2\text{As}_6$  is a multicritical system [37] with several magnetic states accessible by modest magnetic fields. This is the result of having three inequivalent Eu sites in a nonsymmorphic crystal structure [Figs. 1(a), 1(e), and 1(f)] that enables asymmetric exchange interactions [37].

#### D. Colossal magnetoresistance (CMR)

The resistivity data reveal two types of CMR in  $\text{Eu}_5\text{In}_2\text{As}_6$ , one at low temperatures near  $T_{N1}$  associated with a sharp upturn in the resistivity, and another at high temperatures well above  $T_{N1}$  associated with a broad peak in the resistivity. The resistivity upturn and resistivity peak are affected differently by the magnetic field, leading to two distinct types of CMR. Figure 3(a) shows the  $\rho_{zz}(T)$  curves obtained with both current and voltage leads along the crystallographic  $c$  axis. The pink curve is measured at zero field, and the rest of the curves are obtained under different magnetic fields labeled by different colors in the legend of Fig. 3(b). For consistency, we

follow the same color code to specify the magnetic field in Figs. 3(a), 3(b), 3(d), and 3(e).

The blue curve in Fig. 3(a) shows that at 1.5 T,  $\rho_{zz}(T)$  increases as the temperature is decreased from 300 K and forms a broad peak at around 27 K, before it exhibits a sharp upturn at 15.5 K. Looking closely at the blue curve [inset of Fig. 3(a)], one could identify a shallow trough near 24 K between the peak at 27 K and the upturn at 15.5 K. The shallow trough becomes deeper with increasing field but its characteristic temperature does not change. These three features in the resistivity curves, namely, the broad peak at  $T_{\text{peak}}^\rho$ , the trough at  $T_{\text{trough}}^\rho$ , and the upturn at  $T_{\text{up}}^\rho$ , evolve with increasing magnetic field as shown in the inset of Fig. 3(e).

The suppression of the resistivity peak and resistivity upturn in Fig. 3(a) leads to two distinct types of CMR as the field is increased from zero to 9 T. The high-temperature peak-type CMR at  $T_{\text{peak}}^\rho$  spans 3 orders of magnitude while its characteristic temperature  $T_{\text{peak}}^\rho$  increases with increasing field [inset of Fig. 3(e)]. The low-temperature upturn-type CMR is even larger, spanning 7 orders of magnitude. Changing the magnetic field direction from  $H \parallel a$  [Fig. 3(a)] to  $H \parallel c$  [Fig. 3(b)] does not affect either type of CMR. Changing the

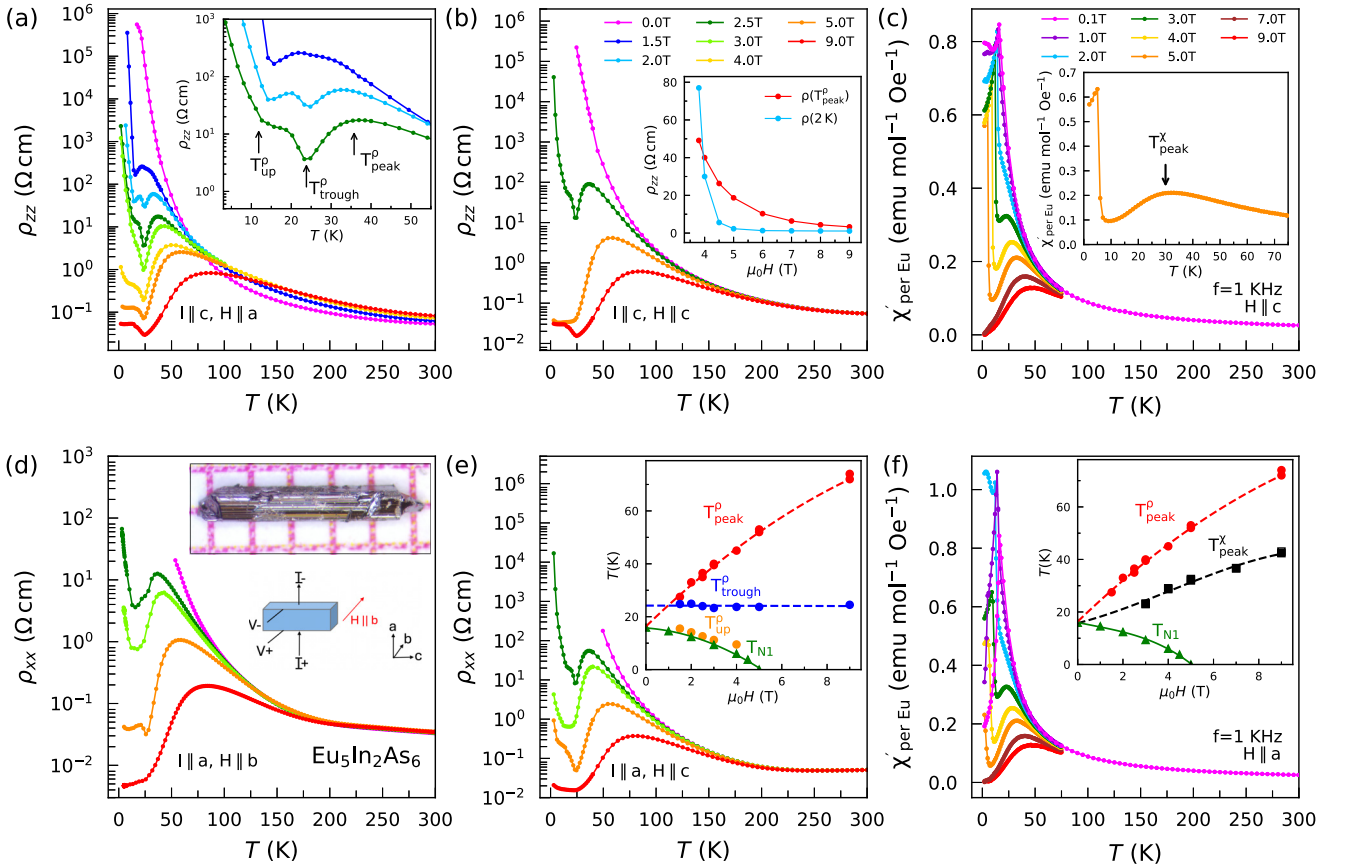


FIG. 3. (a) Resistivity curves measured with current and voltage leads along the  $c$  axis ( $\rho_{zz}$ ) at different fields with  $H \parallel a$ . At zero field,  $\rho_{zz}$  exceeds the detection limit of our instrument below 20 K. The inset magnifies  $\rho_{zz}(T)$  to indicate  $T_{\text{peak}}^{\rho}$ ,  $T_{\text{trough}}^{\rho}$ , and  $T_{\text{up}}^{\rho}$ . (b)  $\rho_{zz}(T)$  measured with  $H \parallel c$  shows similar behavior as with  $H \parallel a$ . The inset highlights the different field dependence between the two types of CMR, namely, the peak-type CMR [ $\rho(T_{\text{peak}}^{\rho})$ ] and upturn-type CMR [ $\rho(2\text{K})$ ]. The  $\rho_{zz}(T)$  data from which this plot is constructed are shown in Fig. S10. (c) The broad peak in the AC susceptibility data at  $T > T_{N1}$  is evidence of polarons. The sharp peak is due to magnetic ordering. (d) Resistivity curves measured with current and field along the  $a$  axis ( $\rho_{xx}$ ) with  $H \parallel b$ . The inset shows a crystal of  $\text{Eu}_5\text{In}_2\text{As}_6$  with the longest dimension being along the  $c$  axis. (e)  $\rho_{xx}(T)$  curves with  $H \parallel c$ . The inset compares the field dependence of  $T_{\text{peak}}^{\rho}$ ,  $T_{\text{trough}}^{\rho}$ , and  $T_{N1}$ . (f) AC susceptibility data with  $H \parallel a$  shows similar behavior as with  $H \parallel c$ . The inset compares the field dependence of  $T_{\text{peak}}^{\rho}$  (circles),  $T_{\text{peak}}^{\chi}$  (squares), and  $T_{N1}$  (triangles).

electric current direction also leaves both types of CMR qualitatively unchanged as seen in the  $\rho_{xx}(T)$  curves with  $H \parallel b$  [Fig. 3(d)] and  $H \parallel c$  [Fig. 3(e)]. Inset of Fig. 3(b) reveals a gradual suppression of the resistivity peak at  $T_{\text{peak}}^{\rho}$  in contrast to the rapid drop in the resistivity upturn at 2 K. Note that the drop in the resistivity upturn is complete by 5.5 T, the field at which the AFM order is fully suppressed [Figs. 2(c) and 2(f)], whereas the suppression of resistivity peak extends to 9 T. Since the peak-type and upturn-type CMRs are marked by different resistivity features, different temperature scales, and different field dependencies, they must have different origins. Below, we will discuss each type in more detail.

**Peak-type CMR.** The broad peak in the resistivity curves at  $T_{\text{peak}}^{\rho}$  could be attributed to magnetic polarons, which are nanometer-size FM clusters of  $\text{Eu}^{2+}$  moments coupled via conduction electrons [38–42]. When the sample is cooled from room temperature to  $T_{\text{peak}}^{\rho}$ , polarons proliferate and grow in size, so they scatter electrons at a higher rate and increase the resistivity. With further decreasing temperature below  $T_{\text{peak}}^{\rho}$ , polarons overlap and provide percolation paths for conduction electrons, so the resistivity decreases. Increasing the

magnetic field makes it easier to polarize the FM clusters, so the polaron peak at  $T_{\text{peak}}^{\rho}$  shifts to higher temperatures with increasing field, as seen in Figs. 3(a), 3(b), 3(d), and 3(e).

The inset of Fig. 3(e) highlights the opposite effect of the magnetic field on magnetic polarons and magnetic order. The red circles mark  $T_{\text{peak}}^{\rho}$  in  $\rho_{zz}(T)$  curves at different fields, while the green triangles mark  $T_{N1}$  from heat capacity data in Fig. 2(e). With increasing field,  $T_{\text{peak}}^{\rho}$  is shifted to higher temperatures because local moments polarize more easily and fluctuate less under an external field. In contrast,  $T_{N1}$  is shifted to lower temperatures since the AFM order is suppressed by the field.

We also find evidence of magnetic polarons in the AC susceptibility data in Figs. 3(c) and 3(f) for  $H \parallel c$  and  $H \parallel a$ , respectively. Since Eu  $f$  moments are localized, a Curie-Weiss behavior ( $\chi' \propto 1/T$ ) is expected at  $T > T_{N1}$ . However, Figs. 3(c) and 3(f) show a deviation from the  $1/T$  behavior with a broad peak at  $T_{\text{peak}}^{\chi}$  [inset of Fig. 3(c)]. The broad peak at  $T_{\text{peak}}^{\chi}$  suggests a reduction of the magnetic susceptibility due to short-range magnetic correlations developing within magnetic polarons.

In both susceptibility and resistivity data, the broad polaronic peaks are shifted to higher temperatures with increasing magnetic field, as shown in the inset of Fig. 3(f). However, the susceptibility peaks occur at lower temperatures compared to the resistivity peaks [ $T_{\text{peak}}^{\chi} < T_{\text{peak}}^{\rho}$  in Fig. 3(f)]. This is because the susceptibility and resistivity reveal two different aspects of polarons. Susceptibility measures the spin correlations within polarons that develop at lower temperatures, while resistivity measures the scattering of conduction electrons by polarons that starts from higher temperatures. Such a difference between transport and thermodynamic quantities has also been reported in  $\text{EuB}_6$ , the archetypal polaronic material [43,44].

**Upturn-type CMR.** The second type of CMR is marked by the 7 orders-of-magnitude suppression of the resistivity upturn at the lowest measured temperature (2 K) as the field increases from zero to 9 T. The inset of Fig. 3(a) shows that the resistivity upturn initiates at  $T_{\text{trough}}^{\rho}$  but then it accelerates by the onset of magnetic ordering at  $T_{\text{up}}^{\rho}$  which coincides with  $T_{\text{N1}}$  [inset of Fig. 3(e)]. At  $T < T_{\text{up}}^{\rho}$ , resistivity continues to increase down to the lowest measured temperatures. As the magnetic order becomes weaker with increasing field, the resistivity upturn also attenuates [Figs. 3(a), 3(b), 3(d), and 3(e)]. Specifically, the inset of Fig. 3(b) shows a near complete suppression of the resistivity upturn by 5.5 T, where the AFM order is fully suppressed. This is consistent with the parallel suppression of  $T_{\text{up}}^{\rho}$  and  $T_{\text{N1}}$  with increasing field from zero to 5.5 T in the inset of Fig. 3(e).

The parallel suppression of the upturn-type CMR and magnetic ordering with increasing field may suggest that the upturn-type CMR is caused by magnetic ordering. However, magnetic ordering typically reduces electrical resistance by removing spin fluctuations as a source of scattering. Thus, we can propose two potential mechanisms for the observed upturn-type CMR. The first possibility is a reconstruction of the electronic structure by the AFM order, i.e., a metal-insulator transition induced by the Slater mechanism [45]. The second possibility is a charge ordering concomitant with AFM ordering, a scenario which is well established in manganese perovskites with CMR [46–48]. The first scenario is challenged by DFT calculations that suggest  $\text{Eu}_5\text{In}_2\text{As}_6$  is a narrow gap semiconductor, so it already has a small gap before entering the AFM phase [20]. The second scenario is challenged by the fact that unlike manganites,  $\text{Eu}_5\text{In}_2\text{As}_6$  is not a Mott insulator, so its physics could be different from those materials. Future ARPES experiments could reveal the band reconstruction [19,49] while x-ray scattering [46] and microwave impedance microscopy [50] could reveal charge ordering.

It is worth noting that the temperature scale  $T_{\text{trough}}^{\rho}$ , where the resistivity upturn initiates, is field independent as shown in the inset of Fig. 3(e). Notably, this feature in resistivity shows no corresponding thermodynamic signature either in magnetization or heat-capacity measurements. Thus, the origin of this feature remains unclear and requires further investigation.

### E. Neutron diffraction

We used neutron diffraction data to resolve the spin structure of the ordered state below  $T_{\text{N1}}$  and  $T_{\text{N2}}$  in  $\text{Eu}_5\text{In}_2\text{As}_6$  at zero field. Figure 4(a) shows the onset of magnetic diffraction

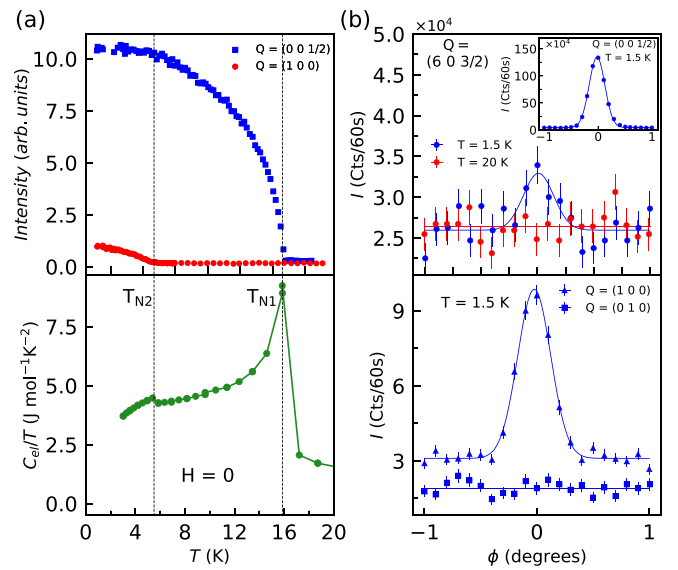


FIG. 4. (a) Temperature dependence of the neutron magnetic Bragg peak intensities at  $\mathbf{Q} = (0, 0, \frac{1}{2})$  and  $(1, 0, 0)$  in the top panel is compared to the temperature dependence of heat capacity in the bottom panel. (b) The top panel shows the intensity of  $\mathbf{Q} = (6, 0, \frac{3}{2})$  peak at both  $T = 1.5$  and 20 K. The inset shows  $\mathbf{Q} = (0, 0, \frac{1}{2})$  peak at  $T = 1.5$  K with much larger intensity than  $\mathbf{Q} = (6, 0, \frac{3}{2})$  peak while both of them correspond to  $\mathbf{k}_1$ . The bottom panel shows that magnetic Bragg scattering is present for  $\mathbf{Q} = (1, 0, 0)$  (triangles) but absent for  $\mathbf{Q} = (0, 1, 0)$  (squares) at  $T = 1.5$  K. Note that the intensity of  $\mathbf{Q} = (1, 0, 0)$  corresponding to  $\mathbf{k}_2$  is about 10 times less than that of  $\mathbf{Q} = (0, 0, \frac{1}{2})$  corresponding to  $\mathbf{k}_1$ .

peaks indexed by a propagation vector  $\mathbf{k}_1 = (0, 0, \frac{1}{2})$  below  $T_{\text{N1}}$  and another set of peaks indexed by  $\mathbf{k}_2 = (0, 0, 0)$  below  $T_{\text{N2}}$ . Given the likelihood of a charge ordering in  $\text{Eu}_5\text{In}_2\text{As}_6$ , we associated this phenomenology to a magnetic phase segregation scenario where  $\mathbf{k}_1$  and  $\mathbf{k}_2$  magnetic domains form separately within the sample. This is consistent with the lack of intensity changes observed at  $\mathbf{Q} = (0, 0, \frac{1}{2})$  when the  $k_2$  peak onsets below  $T_{\text{N2}}$ . The  $\mathbf{k}_1$  wave vector corresponds to an interlayer AFM order along the  $c$  axis, which persists to zero temperature, while  $\mathbf{k}_2$  corresponds to the development of a spin structure with an FM interlayer coupling arising below  $T_{\text{N2}}$ . Note that the peak intensity of  $\mathbf{k}_2$  is about 10 times smaller than  $\mathbf{k}_1$ , indicating that the  $\mathbf{k}_1$  domains form the majority of the sample volume. This can also be appreciated by comparing the rocking scans for  $\mathbf{Q} = (0, 0, \frac{1}{2})$  [inset in the top panel of Fig. 4(b)] and  $\mathbf{Q} = (0, 0, 1)$  [bottom panel of Fig. 4(b)]. For comparison,  $\text{Eu}_5\text{In}_2\text{Sb}_6$  shows a reverse order of wave vectors, such that  $\mathbf{k}_2$  and  $\mathbf{k}_1$  appear with comparable intensities below  $T_{\text{N1}}$  and  $T_{\text{N2}}$ , respectively [13].

Following the symmetry analysis of Refs. [13,15] for  $\text{Eu}_5\text{In}_2\text{Sb}_6$ , we find eight irreducible representations (irreps) for the  $\text{Eu}_5\text{In}_2\text{As}_6$  space group  $Pbam$  compatible with the propagation vectors  $\mathbf{k}_1 = (0, 0, \frac{1}{2})$  and  $\mathbf{k}_2 = (0, 0, 0)$ . However, only four irreps ( $\Gamma_1, \Gamma_3, \Gamma_5, \Gamma_7$ ) can produce magnetization on all three Eu Wyckoff sites, a condition imposed by the full entropy of  $R \ln 8$  in Fig. 1(b). These four irreps correspond to an AFM or FM arrangement of  $\text{Eu}^{2+}$  spins within each  $ab$  plane oriented along either the

$a$  ( $\Gamma_3$ ,  $\Gamma_5$ ),  $b$  ( $\Gamma_3$ ,  $\Gamma_5$ ), or  $c$  ( $\Gamma_1$ ,  $\Gamma_7$ ) directions. The second-order phase transitions revealed by heat-capacity [Fig. 1(b)] and order-parameter measurements [Fig. 4(a)] require a single irrep to explain the magnetic structure.

We first analyze the  $\mathbf{k}_1$  magnetic domains that onset below  $T_{N1}$  and persist to zero temperature with at least 80% volume fraction according to the entropy analysis in Fig. 1(b). As determined by the order-parameter curve collected at  $\mathbf{Q} = (0, 0, \frac{1}{2})$  [Fig. 4(a)], magnetic Bragg peaks for these domains are observed at  $\mathbf{Q} = (0, 0, L)$ . Since neutron scattering only probes magnetization perpendicular to the momentum transfer  $\mathbf{Q}$ , any irrep with spins strictly along the  $c$  direction ( $\Gamma_1$  and  $\Gamma_7$ ) are excluded. This leaves  $\Gamma_3$  and  $\Gamma_5$  as the only viable choices.

$\Gamma_3$  has an FM basis vector with the spins pointing along the  $a$  axis [ $\Gamma_3(\psi_1)$ ], and an AFM basis vector with the spins pointing along the  $b$  axis [ $\Gamma_3(\psi_2)$ ].  $\Gamma_5$  has the opposite spin arrangement, i.e., it has an FM basis vector with spins along the  $b$  axis [ $\Gamma_5(\psi_2)$ ], and an AFM basis vector with spins along the  $a$  axis [ $\Gamma_5(\psi_1)$ ]. An FM order within the  $ab$  plane produces magnetic Bragg peaks at  $\mathbf{Q} = (\text{even}, 0, \frac{L}{2})$ , while an AFM order produces them at  $\mathbf{Q} = (\text{odd}, 0, \frac{L}{2})$ . The top panel of Fig. 4(b) shows magnetic Bragg scattering at even positions, indicating an FM arrangement within the  $ab$  plane. Therefore, the spin structure can be represented by either  $\Gamma_3(\psi_1)$  or  $\Gamma_5(\psi_2)$ . We show the  $\mathbf{Q} = (0, 0, \frac{1}{2})$  rocking scan as inset since its peak intensity is an order of magnitude larger than the  $\mathbf{Q} = (6, 0, \frac{3}{2})$  peak in the main panel.

A quantitative refinement of the Bragg peak intensities could distinguish between  $\Gamma_3(\psi_1)$  and  $\Gamma_5(\psi_2)$ , but this contrast disappears due to the large neutron absorption cross sections of Eu. However, the  $\Gamma_3(\psi_1)$  basis vector is consistent with the low-temperature magnetization of  $\text{Eu}_5\text{In}_2\text{As}_6$  [Fig. 1(d)], which shows spin-flop transitions for field applied along the  $a$  axis. This contrasts with the magnetization for a field applied along the  $b$  axis where such spin-flop transitions are not observed and would be expected to occur for the  $\Gamma_5(\psi_2)$  structure. Therefore, we conclude that  $\Gamma_3(\psi_1)$  is the appropriate irrep to describe the magnetic domains forming below  $T_{N1}$  in  $\text{Eu}_5\text{In}_2\text{As}_6$ . This irrep also describes the low-temperature magnetic phase of  $\text{Eu}_5\text{In}_2\text{Sb}_6$  [13,15]. We depict the resulting  $\mathbf{k}_1$  magnetic domains in Fig. 1(e).

We next turn our attention to the details of the  $\mathbf{k}_2$  magnetic domains. Our bulk magnetization data in Fig. 1(c) shows a hysteresis loop opening below  $T_{N2}$ , indicating a net FM component along the  $a$  axis. We also detected magnetic Bragg peaks at structurally nonallowed Bragg positions, such as  $\mathbf{Q} = (1, 0, 0)$  plotted in the bottom panel of Fig. 4(b). This indicates that the  $\mathbf{k}_2 = (0, 0, 0)$  domains also have an AFM component within the  $ab$  plane. Since no magnetic Bragg peaks were found at  $\mathbf{Q} = (0, H, 0)$  positions [Fig. 4(b), bottom panel], the spin polarization of this AFM component is along the  $b$  axis. Thus, the magnetic structure below  $T_{N2}$  must have a net FM component along the  $a$  axis and an AFM component along the  $b$  axis. This means the irrep for the  $\mathbf{k}_2 = (0, 0, 0)$  domains are identical to the ones for  $\mathbf{k}_1 = (0, 0, \frac{1}{2})$ , but the spins do not reverse going along the

$c$  direction [13,15]. The spin structure for the  $\mathbf{k}_2$  domains is represented in Fig. 1(f).

Finally, we note that our neutron diffraction data cannot distinguish a multi- $\mathbf{k}$  structure from our proposed magnetic phase segregation scenario as they both lead to identical zero-field neutron diffraction patterns. A magnetic phase separation between the same AFM-1 and AFM-0 domains was also suggested for  $\text{Eu}_5\text{In}_2\text{Sb}_6$  [15], but in this latter compound the AFM-0 state forms the majority domains. Furthermore, we propose that a phase separation is quite likely if charge ordering or segregation is responsible for the upturn-type CMR. The competition between charge order and AFM order over the same carriers leads to enhanced scattering of conduction electrons, giving rise to the resistivity upturn. With increasing field, both charge and AFM order are suppressed, giving rise to the upturn-type CMR. Future studies using magnetic imaging techniques may reveal magnetic and charge phase separation in  $\text{Eu}_5\text{In}_2\text{As}_6$ .

In the Supplemental Material, we provide  $\mu\text{SR}$  data (Fig. S6) that are also consistent with a phase separation scenario.  $\mu\text{SR}$  is a sensitive probe of the local magnetic environment and local field distribution, so it provides additional insight into the magnetic state of  $\text{Eu}_5\text{In}_2\text{As}_6$ . However, for completeness, we also discuss the multi- $\mathbf{k}$  scenario in the Supplemental Material (Fig. S7) [24].

#### IV. SUMMARY AND OUTLOOK

The two types of CMR discussed here have been observed in different Zintl compounds but they were not explained in a unifying manner. For example,  $\text{CeSb}_{0.1}\text{Te}_{1.9}$ ,  $\text{EuAuSb}$ , and  $\text{EuCd}_2\text{As}_2$  show the peak-type CMR [4,17,18] whereas  $\text{EuCd}_2\text{P}_2$ ,  $\text{Mn}_3\text{Si}_2\text{Te}_6$ , and  $\text{Eu}_5\text{In}_2\text{Sb}_6$  show both the peak-type CMR and the upturn-type CMR [8,11,16]. Based on the similarity of transport data across different Zintl compounds, we argue that similar mechanisms are at work to produce the two types of CMR in these materials. Specifically, we attribute the peak-type CMR to percolation of magnetic polarons and the upturn-type CMR to either melting of a charge ordered state or band structure reconstruction by the AFM order (Slater mechanism).

The relationship between polarons and CMR has been well established in metallic systems such as  $\text{EuB}_6$  [44]. Our work demonstrates that polaron formation is not limited to the metallic regime and can be found in the semiconducting regime as well. Similarly, charge ordering in manganites happens in the metallic regime [47], but our work extends it to the semiconducting regime with small concentration of extrinsic carriers, which is the case in  $\text{Eu}_5\text{In}_2\text{As}_6$ . Charge ordering has recently been reported in  $\text{EuTe}_4$ , another semiconductor with comparable carrier concentration and band gap to  $\text{Eu}_5\text{In}_2\text{As}_6$  [51,52].

The resistivity of  $\text{Eu}_5\text{In}_2\text{As}_6$  shows similar trends to those observed in  $\text{EuX}$  ( $X = \text{O}, \text{S}, \text{Se}, \text{Te}$ ) [53–59]. In  $\text{EuSe}$ , it has been argued that the low-temperature upturn is due to the trapping of electrons caused by strong  $s$ - $f$  hybridization. This charge trapping can be suppressed by a magnetic field, as the field polarizes the  $f$  electrons [55]. We observe a similar

influence of the magnetic field on charge ordering, as depicted in the inset of Fig. 3(e). It is worth noting that our use of the term “charge order” is somewhat broad and may also encompass “charge segregation,” in the sense that different magnetic domains could have varying charge densities. As the magnetic field increases, the magnetic domains align, and the charge segregation weakens.

The CMR induced by magnetic polarons implies a coupling between short-range FM ordering and charge transport, while the CMR associated with charge ordering reflects a coupling between long-range AFM ordering and charge transport. Such an intricate interplay between magnetism (both long and short range) and the charge transport is a key feature of many Eu-based Zintl phases [9,15,60], potentially driven by the large spin of  $\text{Eu}^{2+}$  and considerable magnetoelastic coupling. It is noteworthy that a strong influence of the  $4f$  states of europium, through their coupling to valence and conduction states, on the band structure and charge transport of  $\text{EuCd}_2\text{X}_2$  ( $X = \text{P,As,Sb}$ ) systems has already been demonstrated [49,61].

An indirect manifestation of magnetoelastic coupling is the dependence of the magnetic state of Eu-based Zintl compounds on the choice of flux in crystal growth [5,62]. These characteristics position Eu-based CMR materials as promising candidates for magnetic sensing, spin valve, and piezoresistive technologies [12].

In the Supplemental Material Fig. S8 [24], we present an Arrhenius analysis on the zero-field resistivity data from two samples of  $\text{Eu}_5\text{In}_2\text{As}_6$  revealing significantly different activation gaps of 35 and 125 meV in samples S1 and S2, respectively. Hall effect data in Fig. S8 reveal different  $n$ -type carrier concentrations in samples S1 ( $10^{18} \text{ cm}^{-3}$ ) and S2 ( $10^{16} \text{ cm}^{-3}$ ), so the sample with a larger gap (S1) shows a smaller carrier concentration. The different gap values and carrier concentrations in different samples suggest that  $\text{Eu}_5\text{In}_2\text{As}_6$  is a self-doped semiconductor. Remarkably, all the interesting transport phenomena in this material, and possibly

other Eu-based CMR materials, seem to originate from a small density of extrinsic carriers.

## ACKNOWLEDGMENTS

The work at Boston College was funded by the U.S. Department of Energy, Office of Basic Energy Sciences, Division of Physical Behavior of Materials under award number DE-SC0023124. This material is based upon work supported by the Air Force Office of Scientific Research under Awards No. FA2386-21-1-4059 and No. FA9550-23-1-0124. A.R. acknowledges support from the Swedish Research Council, Grant No. 2021-04360. A portion of this work was performed at the National High Magnetic Field Laboratory, which is supported by the National Science Foundation Cooperative Agreement No. DMR-1644779 and the state of Florida. The support for neutron scattering was provided by the Center for High-Resolution Neutron Scattering, a partnership between the National Institute of Standards and Technology and the National Science Foundation under Agreement No. DMR-2010792. The identification of any commercial product or trade name does not imply endorsement or recommendation by the National Institute of Standards and Technology. A portion of this research used resources at the High Flux Isotope Reactor, a DOE Office of Science User Facility operated by the Oak Ridge National Laboratory. The beam time was allocated to VERITAS on Proposal No. IPTS-31509. Part of this work is based on experiments carried out at the Swiss Muon Source  $S\mu\text{S}$ , Paul Scherrer Institute, Villigen, Switzerland. We thank E. Kenney for assistance with the  $\mu\text{SR}$  data analysis.

## DATA AVAILABILITY

The data that support the findings of this article are openly available [63]; embargo periods may apply.

- 
- [1] V. Baltz, A. Manchon, M. Tsoi, T. Moriyama, T. Ono, and Y. Tserkovnyak, Antiferromagnetic spintronics, *Rev. Mod. Phys.* **90**, 015005 (2018).
- [2] J. Han, R. Cheng, L. Liu, H. Ohno, and S. Fukami, Coherent antiferromagnetic spintronics, *Nat. Mater.* **22**, 684 (2023).
- [3] J. Xu, J. He, J.-S. Zhou, D. Qu, S.-Y. Huang, and C. L. Chien, Observation of vector spin seebeck effect in a noncollinear antiferromagnet, *Phys. Rev. Lett.* **129**, 117202 (2022).
- [4] J.-Z. Ma, S. M. Nie, C. J. Yi, J. Jandke, T. Shang, M. Y. Yao, M. Naamneh, L. Q. Yan, Y. Sun, A. Chikina, V. N. Strocov, M. Medarde, M. Song, Y.-M. Xiong, G. Xu, W. Wulfhelk, J. Mesot, M. Reticioli, C. Franchini, C. Mudry *et al.*, Spin fluctuation induced Weyl semimetal state in the paramagnetic phase of  $\text{EuCd}_2\text{As}_2$ , *Sci. Adv.* **5**, eaaw4718 (2019).
- [5] N. H. Jo, B. Kuthanazhi, Y. Wu, E. Timmons, T.-H. Kim, L. Zhou, L.-L. Wang, B. G. Ueland, A. Palasyuk, D. H. Ryan, R. J. McQueeney, K. Lee, B. Schruck, A. A. Burkov, R. Prozorov, S. L. Bud'ko, A. Kaminski, and P. C. Canfield, Manipulating magnetism in the topological semimetal  $\text{EuCd}_2\text{As}_2$ , *Phys. Rev. B* **101**, 140402(R) (2020).
- [6] Y. Xu, Z. Song, Z. Wang, H. Weng, and X. Dai, Higher-order topology of the axion insulator  $\text{EuIn}_2\text{As}_2$ , *Phys. Rev. Lett.* **122**, 256402 (2019).
- [7] S. X. M. Riberolles, T. V. Trevisan, B. Kuthanazhi, T. W. Heitmann, F. Ye, D. C. Johnston, S. L. Bud'ko, D. H. Ryan, P. C. Canfield, A. Kreyssig, A. Vishwanath, R. J. McQueeney, L.-L. Wang, P. P. Orth, and B. G. Ueland, Magnetic crystalline-symmetry-protected axion electrodynamics and field-tunable unpinned Dirac cones in  $\text{EuIn}_2\text{As}_2$ , *Nat. Commun.* **12**, 999 (2021).
- [8] Z.-C. Wang, J. D. Rogers, X. Yao, R. Nichols, K. Atay, B. Xu, J. Franklin, I. Sochnikov, P. J. Ryan, D. Haskel, and F. Tafti, Colossal magnetoresistance without mixed valence in a layered phosphide crystal, *Adv. Mater.* **33**, 2005755 (2021).
- [9] V. Sunko, Y. Sun, M. Vranas, C. C. Homes, C. Lee, E. Donoway, Z.-C. Wang, S. Balguri, M. B. Mahendru, A. Ruiz, B. Gunn, R. Basak, S. Blanco-Canosa, E. Schierle, E. Weschke, F. Tafti, A. Frano, and J. Orenstein, Spin-carrier coupling induced ferromagnetism and giant resistivity peak in  $\text{EuCd}_2\text{P}_2$ , *Phys. Rev. B* **107**, 144404 (2023).

- [10] C. C. Homes, Z.-C. Wang, K. Fruhling, and F. Tafti, Optical properties and carrier localization in the layered phosphide  $\text{EuCd}_2\text{P}_2$ , *Phys. Rev. B* **107**, 045106 (2023).
- [11] P. Rosa, Y. Xu, M. Rahn, J. Souza, S. Kushwaha, L. Veiga, A. Bombardi, S. Thomas, M. Janoschek, E. Bauer, M. Chan, Z. Wang, J. Thompson, N. Harrison, P. Pagliuso, A. Bernevig, and F. Ronning, Colossal magnetoresistance in a nonsymmorphic antiferromagnetic insulator, *npj Quantum Mater.* **5**, 52 (2020).
- [12] S. Ghosh, C. Lane, F. Ronning, E. D. Bauer, J. D. Thompson, J.-X. Zhu, P. F. S. Rosa, and S. M. Thomas, Colossal piezoresistance in narrow-gap  $\text{Eu}_5\text{In}_2\text{Sb}_6$ , *Phys. Rev. B* **106**, 045110 (2022).
- [13] V. C. Morano, J. Gaudet, N. Varnava, T. Berry, T. Halloran, C. J. Lygouras, X. Wang, C. M. Hoffman, G. Xu, J. W. Lynn, T. M. McQueen, D. Vanderbilt, and C. L. Broholm, Noncollinear 2k antiferromagnetism in the Zintl semiconductor  $\text{Eu}_5\text{In}_2\text{Sb}_6$ , *Phys. Rev. B* **109**, 014432 (2024).
- [14] J. C. Souza, S. M. Thomas, E. D. Bauer, J. D. Thompson, F. Ronning, P. G. Pagliuso, and P. F. S. Rosa, Microscopic probe of magnetic polarons in antiferromagnetic  $\text{Eu}_5\text{In}_2\text{Sb}_6$ , *Phys. Rev. B* **105**, 035135 (2022).
- [15] M. C. Rahn, M. N. Wilson, T. J. Hicken, F. L. Pratt, C. Wang, F. Orlandi, D. D. Khalyavin, P. Manuel, L. S. I. Veiga, A. Bombardi, S. Francoual, P. Bereciartua, A. S. Sukhanov, J. D. Thompson, S. M. Thomas, P. F. S. Rosa, T. Lancaster, F. Ronning, and M. Janoschek, Magnetism in the axion insulator candidate  $\text{Eu}_5\text{In}_2\text{Sb}_6$ , *Phys. Rev. B* **109**, 174404 (2024).
- [16] Y. Zhang, Y. Ni, H. Zhao, S. Hakani, F. Ye, L. DeLong, I. Kimchi, and G. Cao, Control of chiral orbital currents in a colossal magnetoresistance material, *Nature (London)* **611**, 467 (2022).
- [17] R. Singha, K. J. Dalgaard, D. Marchenko, M. Krivenkov, E. D. L. Rienks, M. Jovanovic, S. M. L. Teicher, J. Hu, T. H. Salters, J. Lin, A. Varykhalov, N. P. Ong, and L. M. Schoop, Colossal magnetoresistance in the multiple wave vector charge density wave regime of an antiferromagnetic Dirac semimetal, *Sci. Adv.* **9**, eadh0145 (2023).
- [18] D. Ram, J. Singh, S. Banerjee, A. Sundaresan, D. Samal, V. Kanchana, and Z. Hossain, Magnetotransport and electronic structure of  $\text{EuAuSb}$ : A candidate antiferromagnetic Dirac semimetal, *Phys. Rev. B* **109**, 155152 (2024).
- [19] H. Zhang, F. Du, X. Zheng, S. Luo, Y. Wu, H. Zheng, S. Cui, Z. Sun, Z. Liu, D. Shen, M. Smidman, Y. Song, M. Shi, Z. Zhong, C. Cao, H. Yuan, and Y. Liu, Electronic band reconstruction across the insulator-metal transition in colossally magnetoresistive  $\text{EuCd}_2\text{P}_2$ , *Phys. Rev. B* **108**, L241115 (2023).
- [20] N. Varnava, T. Berry, T. M. McQueen, and D. Vanderbilt, Engineering magnetic topological insulators in  $\text{Eu}_5\text{M}_2\text{X}_6$  Zintl compounds, *Phys. Rev. B* **105**, 235128 (2022).
- [21] N. Tomitaka, Y. Goto, K. Morino, K. Hoshi, Y. Nakahira, H. Ito, A. Miura, H. Usui, and Y. Mizuguchi, Bipolar doping and thermoelectric properties of Zintl arsenide  $\text{Eu}_5\text{In}_2\text{As}_6$ , *J. Mater. Chem. A* **9**, 26362 (2021).
- [22] M. Radzieowski, F. Stegemann, S. Klenner, Y. Zhang, B. P. T. Fokwa, and O. Janka, On the divalent character of the Eu atoms in the ternary Zintl phases  $\text{Eu}_5\text{In}_2\text{Pn}_6$  and  $\text{Eu}_3\text{MAs}_3$  ( $\text{Pn} = \text{As}-\text{Bi}$ ;  $\text{M} = \text{Al}, \text{Ga}$ ), *Mater. Chem. Front.* **4**, 1231 (2020).
- [23] E. A. Stern, Theory of the anharmonic properties of solids, *Phys. Rev.* **111**, 786 (1958).
- [24] See Supplemental Material at <http://link.aps.org/supplemental/10.1103/PhysRevB.111.115114> for additional information about crystal growth, Curie-Weiss analysis, low-temperature specific heat, tunnel diode oscillations, and transport data.
- [25] J. Rodríguez-Carvajal, Recent advances in magnetic structure determination by neutron powder diffraction, *Phys. B: Condens. Matter* **192**, 55 (1993).
- [26] K. Momma and F. Izumi, VESTA 3 for three-dimensional visualization of crystal, volumetric and morphology data, *J. Appl. Crystallogr.* **44**, 1272 (2011).
- [27] A. S. Wills, A new protocol for the determination of magnetic structures using simulated annealing and representational analysis (SARA $h$ ), *Phys. B: Condens. Matter* **276-278**, 680 (2000).
- [28] N. J. Chesser and J. D. Axe, Derivation and experimental verification of the normalized resolution function for inelastic neutron scattering, *Acta Crystallogr. Sect. A* **29**, 160 (1973).
- [29] B. J. Wuensch and C. T. Prewitt, Corrections for x-ray absorption by a crystal of arbitrary shape, *Z. Kristallogr.-Cryst. Mater.* **122**, 24 (1965).
- [30] A. Amato, H. Luetkens, K. Sedlak, A. Stoykov, R. Scheuermann, M. Elender, A. Raselli, and D. Graf, The new versatile general purpose surface-muon instrument (GPS) based on silicon photomultipliers for  $\mu\text{SR}$  measurements on a continuous-wave beam, *Rev. Sci. Instrum.* **88**, 093301 (2017).
- [31] S. M. Kauzlarich, Zintl phases: From curiosities to impactful materials, *Chem. Mater.* **35**, 7355 (2023).
- [32] A. B. Childs, S. Baranets, and S. Bobev, Five new ternary indium-arsenides discovered. Synthesis and structural characterization of the Zintl phases  $\text{Sr}_3\text{In}_2\text{As}_4$ ,  $\text{Ba}_3\text{In}_2\text{As}_4$ ,  $\text{Eu}_3\text{In}_2\text{As}_4$ ,  $\text{Sr}_5\text{In}_2\text{As}_6$  and  $\text{Eu}_5\text{In}_2\text{As}_6$ , *J. Solid State Chem.* **278**, 120889 (2019).
- [33] B. J. Wieder, B. Bradlyn, Z. Wang, J. Cano, Y. Kim, H.-S. D. Kim, A. M. Rappe, C. L. Kane, and B. A. Bernevig, Wallpaper fermions and the nonsymmorphic Dirac insulator, *Science* **361**, 246 (2018).
- [34] M. V. Ale Crivillero, S. Rößler, S. Granovsky, M. Doerr, M. S. Cook, P. F. S. Rosa, J. Müller, and S. Wirth, Magnetic and electronic properties unveil polaron formation in  $\text{Eu}_5\text{In}_2\text{Sb}_6$ , *Sci. Rep.* **13**, 1597 (2023).
- [35] M. V. A. Crivillero, S. Rößler, P. F. S. Rosa, J. Müller, U. K. Rößler, and S. Wirth, Surface and electronic structure at atomic length scales of the nonsymmorphic antiferromagnet  $\text{Eu}_5\text{In}_2\text{Sb}_6$ , *Phys. Rev. B* **106**, 035124 (2022).
- [36] S. Tagliati, V. M. Krasnov, and A. Rydh, Differential membrane-based nanocalorimeter for high-resolution measurements of low-temperature specific heat, *Rev. Sci. Instrum.* **83**, 055107 (2012).
- [37] L.-L. Wang, H. C. Po, R.-J. Slager, and A. Vishwanath, Topological descendants of a multicritical Dirac semimetal with magnetism and strain, *Phys. Rev. B* **104**, 165107 (2021).
- [38] M. Pohlitz, S. Rößler, Y. Ohno, H. Ohno, S. von Molnár, Z. Fisk, J. Müller, and S. Wirth, Evidence for ferromagnetic clusters in the colossal-magnetoresistance material  $\text{EuB}_6$ , *Phys. Rev. Lett.* **120**, 257201 (2018).
- [39] P. Das, A. Amyan, J. Brandenburg, J. Müller, P. Xiong, S. von Molnár, and Z. Fisk, Magnetically driven electronic phase separation in the semimetallic ferromagnet  $\text{EuB}_6$ , *Phys. Rev. B* **86**, 184425 (2012).

- [40] S. Söllow, I. Prasad, S. Bogdanovich, M. C. Aronson, J. L. Sarrao, and Z. Fisk, Magnetotransport in the low carrier density ferromagnet  $\text{EuB}_6$ , *J. Appl. Phys.* **87**, 5591 (2000).
- [41] X. Zhang, L. Yu, S. von Molnár, Z. Fisk, and P. Xiong, Non-linear Hall effect as a signature of electronic phase separation in the semimetallic ferromagnet  $\text{EuB}_6$ , *Phys. Rev. Lett.* **103**, 106602 (2009).
- [42] H. Murakawa, Y. Nakaoka, K. Iwase, T. Kida, M. Hagiwara, H. Sakai, and N. Hanasaki, Giant negative magnetoresistance in the layered semiconductor  $\text{CeTe}_{2-x}\text{Sb}_x$  with variable magnetic polaron density, *Phys. Rev. B* **107**, 165138 (2023).
- [43] R. S. Manna, P. Das, M. de Souza, F. Schnelle, M. Lang, J. Müller, S. von Molnár, and Z. Fisk, Lattice strain accompanying the colossal magnetoresistance effect in  $\text{EuB}_6$ , *Phys. Rev. Lett.* **113**, 067202 (2014).
- [44] J. Chatterjee, U. Yu, and B. I. Min, Spin-polaron model: Transport properties of  $\text{EuB}_6$ , *Phys. Rev. B* **69**, 134423 (2004).
- [45] J. C. Slater, Magnetic effects and the Hartree-Fock equation, *Phys. Rev.* **82**, 538 (1951).
- [46] Y. Tomioka, A. Asamitsu, H. Kuwahara, Y. Moritomo, M. Kasai, R. Kumai, and Y. Tokura, Magnetic-field-induced metal-insulator transition in perovskite-type manganese oxides, *Phys. B: Condens. Matter* **237-238**, 6 (1997).
- [47] Y. Tomioka, A. Asamitsu, Y. Moritomo, H. Kuwahara, and Y. Tokura, Collapse of a charge-ordered state under a magnetic field in  $\text{Pr}_{1/3}\text{Sr}_{2/3}\text{MnO}_3$ , *Phys. Rev. Lett.* **74**, 5108 (1995).
- [48] C. N. R. Rao, Charge, Spin, and orbital ordering in the perovskite manganates,  $\text{Ln}_{1-x}\text{A}_x\text{MnO}_3$  ( $\text{Ln}$  = Rare Earth,  $\text{A}$  = Ca or Sr), *J. Phys. Chem. B* **104**, 5877 (2000).
- [49] Y.-F. Li, E. M. Been, S. Balguri, C.-J. Jia, M. B. Mahendru, Z.-C. Wang, Y. Cui, S.-D. Chen, M. Hashimoto, D.-H. Lu, B. Moritz, J. Zaenen, F. Tafti, T. P. Devereaux, and Z.-X. Shen, Colossal magnetoresistance from spin-polarized polarons in an Ising system, *Proc. Natl. Acad. Sci. USA* **121**, e2409846121 (2024).
- [50] K. Lai, M. Nakamura, W. Kundhikanjana, M. Kawasaki, Y. Tokura, M. A. Kelly, and Z.-X. Shen, Mesoscopic percolating resistance network in a strained manganite thin film, *Science* **329**, 190 (2010).
- [51] D. Wu, Q. M. Liu, S. L. Chen, G. Y. Zhong, J. Su, L. Y. Shi, L. Tong, G. Xu, P. Gao, and N. L. Wang, Layered semiconductor  $\text{EuTe}_4$  with charge density wave order in square tellurium sheets, *Phys. Rev. Mater.* **3**, 024002 (2019).
- [52] B. Q. Lv, A. Zong, D. Wu, A. V. Rozhkov, B. V. Fine, S.-D. Chen, M. Hashimoto, D.-H. Lu, M. Li, Y.-B. Huang, J. P. C. Ruff, D. A. Walko, Z. H. Chen, I. Hwang, Y. Su, X. Shen, X. Wang, F. Han, H. C. Po, Y. Wang *et al.*, Unconventional hysteretic transition in a charge density wave, *Phys. Rev. Lett.* **128**, 036401 (2022).
- [53] Y. Shapira, S. Foner, and T. B. Reed, EuO. I. resistivity and Hall effect in fields up to 150 kOe, *Phys. Rev. B* **8**, 2299 (1973).
- [54] Y. Shapira and T. B. Reed, Resistivity and Hall effect of  $\text{EuS}$  in fields up to 140 kOe, *Phys. Rev. B* **5**, 4877 (1972).
- [55] Y. Shapira, S. Foner, N. F. Oliveira, and T. B. Reed, Resistivity and Hall effect of  $\text{EuSe}$  in fields up to 150 kOe, *Phys. Rev. B* **10**, 4765 (1974).
- [56] Y. Shapira, S. Foner, N. F. Oliveira, and T. B. Reed,  $\text{EuTe}$ . II. resistivity and Hall effect, *Phys. Rev. B* **5**, 2647 (1972).
- [57] V. G. Storchak, O. E. Parfenov, J. H. Brewer, P. L. Russo, S. L. Stubbs, R. L. Lichti, D. G. Eshchenko, E. Morenzoni, S. P. Cottrell, J. S. Lord, T. G. Aminov, V. P. Zlomanov, A. A. Vinokurov, R. L. Kallaher, and S. von Molnár, Electron localization into magnetic polaron in  $\text{EuS}$ , *Phys. B: Condens. Matter* **404**, 896 (2009).
- [58] V. G. Storchak, D. G. Eshchenko, E. Morenzoni, N. Ingle, W. Heiss, T. Schwarzl, G. Springholz, R. L. Kallaher, and S. von Molnár, Magnetic polarons in Eu-based films of magnetic semiconductors, *Phys. Rev. B* **81**, 153201 (2010).
- [59] S. C. P. van Kooten and A. B. Henriques, Experimental evidence for ultrashort-lived spin polarons in  $\text{EuSe}$ , *AIP Adv.* **14**, 025006 (2024).
- [60] M. C. Rahn, J.-R. Soh, S. Francoual, L. S. I. Veiga, J. Stremper, J. Mardegan, D. Y. Yan, Y. F. Guo, Y. G. Shi, and A. T. Boothroyd, Coupling of magnetic order and charge transport in the candidate Dirac semimetal  $\text{EuCd}_2\text{As}_2$ , *Phys. Rev. B* **97**, 214422 (2018).
- [61] S. Nasrallah, D. Santos-Cottin, F. Le Mardelé, I. Mohelský, J. Wyzula, L. Akšamović, P. Sačer, J. W. H. Barrett, W. Galloway, K. Rigaux, F. Guo, M. Puppini, I. Živković, J. H. Dil, M. Novak, C. C. Homes, M. Orlita, N. Barišić, and A. Akrap, Magneto-optical response of the magnetic semiconductors  $\text{EuCd}_2\text{X}_2$  ( $\text{X} = \text{P}, \text{As}, \text{Sb}$ ), *Phys. Rev. B* **110**, L201201 (2024).
- [62] X. Chen, Z. Wang, Z. Zhou, W. Yang, Y. Liu, J.-Y. Lu, Z. Ren, G.-H. Cao, F. Tafti, S. Dong, and Z.-C. Wang, Manipulating magnetism and transport properties of  $\text{EuCd}_2\text{P}_2$  with a low carrier concentration, *Phys. Rev. B* **109**, 224428 (2024).
- [63] See <https://acdc.alcf.anl.gov/mdf/detail/4d144568-261d-4834-a01c-c4841391ef3b-1.0/>